American Society of
Mechanical Engineers

ASME Accepted Manuscript Repository

Extending Highly Loaded Axial Fan Operability Range Through Novel Blade Design

Diego I. Lopez,* **Tiziano Ghisu**
Department of Mechanical, Chemical and Materials Engineering
University of Cagliari
Cagliari, 09123, Italy
Email: diegoi.lopez@unica.it, t.ghisu@unica.it

Timoleon Kipouros
Centre for Propulsion Engineering
University of Cranfield
Cranfield, United Kingdom,
Email: t.kipouros@cranfield.ac.uk

Shahrokh Shahpar
Innovation Hub, Future Methods
Rolls-Royce plc
Derby, United Kingdom,
Email: shahrokh.shahpar@rolls-royce.com

Mark Wilson
Civil Aerospace Division
Rolls-Royce plc
Derby, United Kingdom,
Email: mark.wilson@rolls-royce.com

ABSTRACT

The tip clearance size has historically been considered to be the main factor affecting stability range in axial fan and compressors. This paper reveals that the stall characteristics are defined by the axial momentum flux of the tip leakage flow and that tip clearance is primarily a strong driver for this metric. A bespoke methodology for carefully tailoing the

──────────
*Address all correspondence to this author.

axial momentum via three-dimensional design is presented, which enables a higher degree of control over the stability range for cases where the tip clearance responds to other considerations and cannot be defined for this purpose. The effect of the axial momentum on efficiency is also addressed and the trade-off between operability range and design point performance derived. The results show that that the conditions for optimal stability differ from those for optimal efficiency and that control over the axial momentum enables tuning the design for a desired exchange. Numerical simulations have been employed to drive the analysis through a high-fidelity computational model whose behavior is supported by rich set of experimental data. Contrary to current belief, results further indicate that an accurate characterization of stall, including onset mechanism, can be achieved through steady-state simulations, minimising the need for expensive time-accurate computations during the design phase.

INTRODUCTION

Rotating stall is an unstable regime of fan and compressor operation whereby the presence of non-axisymmetric disturbances prevents the uniform flow of mass through the machine, limiting the extent to which it can be safely operated. The stall margin of a fan or compressor defines the range of stable operation and is a major safety criterion that designers need to take into account for a safe operation of the jet engine and also for a successful certification.

Upon first appearance, the flow disturbances grow and propagate around the annulus and stall is said to occur when their effect is sufficient to promote flow breakdown. Two main paths into breakdown have been identified, distinguishable by their signatures in the pressure/velocity traces and commonly referred to as *modal oscillations* and *spikes* [1,2]. Modal oscillations are employed to describe the occurrence of low-amplitude periodic axial velocity fluctuations with length scales the order of the compressor circumference. Such oscillations cause localized increases in blade incidence at certain parts of the annulus that can drive the loading beyond critical values and lead to the formation of stall cells. Modal flow oscillations can be detected in a machine many revolutions prior to stall and can develop smoothly into stall cells that span a large sector of the

annulus. This sequence is commonly associated with conditions at, or to the left of, the peak of the total-to-static pressure characteristic [3, 4] and the initial stages of its evolution, where the amplitude remains small, can be well explained through linear models [5, 6].

However, modern compression systems employ highly optimized blades with reduced losses and blockage and typically do not experience a peak of the pressure-rise characteristic. In addition, design trends favour highly loaded blades, for which minor distortions in the incoming flow, or blade shape deviations, can drive the incidence beyond critical values when operating at a point on the the right side of the characteristic [7, 8]. On such scenarios pre-stall waves are not observed [2]. Thus, the more frequent path into instability for modern fans and compressors is characterized by smaller scale (a few blade pitches) transients, called spikes, which appear as sharp oscillations in the pressure traces and propagate circumferentially at speeds about 70% to 80% of the rotor speed [9]. The amplitude of these distortions is larger compared to the mean flow velocity and they can grow into fully-formed stall cells within about three rotor revolutions.

Many research efforts have been dedicated to defining the characteristics of spikes and the fluid mechanisms that lead to their formation in core compressors [10–13] and fan blades [14–16]. The onset of these disturbances has been shown to be primarily linked to the tip aerodynamics, where flow separation from the leading edge (LE) begins due to high incidence. This condition needs only to be present at a single blade to initiate the unstable evolution towards rotating stall. The vorticity shed from the separated flow rolls up into a vortex tube that is bounded by the blade suction surface on one end and the casing on the other, and it propagates circumferentially [17]. The convecting vortex creates blockage in the passage, which increases incidence of the adjacent blade and thus constitutes a positive feedback loop for the propagation and growth of the instability.

Vo *et al*. [10], suggest two criteria that promote high incidence and the formation of a spike-type disturbance, both linked to over tip leakage flow. The first condition is spillage of the leakage jet ahead of the adjacent blade's LE and below the tip radius. The second involves tip leakage fluid from an adjacent blade passage impinging on the pressure surface at the trailing edge, which creates flow reversal and corner separation.

Pullan *et al*. [11], showed that while tip leakage spillage is a primary mechanism contributing

to the formation of spikes, these disturbances can also occur in the absence of any leakage flow. The study detected spikes on rotors without tip clearance, suggesting a secondary mechanism that drives their formation. Shock-boundary layer interactions at the tip region cause separation downstream of the shock that create blockage. As the mass flow is reduced, blockage in the passage grows and reaches the casing, forming a corner separation and triggering the formation of a spike.

By analysing an array of compressor configurations with varying tip gaps, Hewkin-Smith *et al*. [13] found interactions between the two competing mechanisms and their correlation to the tip gap size. At low clearance values, casing corner separation is the leading cause of spike formation. However, as the gap is opened up, leakage fluid energizes the boundary layer and interrupts the passage blockage from reaching the casing, delaying stall onset. Further increases in the tip gap size, however, increase the axial momentum of the leakage flow and contributes to early spillage, initiating the formation of spikes. They found thus a non-zero tip clearance that is optimal in extending the stability range to lower mass flows.

Kim *et al*. [16], studied the different spike-inducing mechanisms on fan blades and found that the radial distribution of loading has an effect on the final size of the stall cell but not necessarily the path to spike formation. The study assessed two fan blades that operated at similar pressure ratios at design point, but presented different loading distributions, one approximately uniform and the second with a marked decay in the tip region. Their results show that the fan with uniform loading was more prone to spikes initiated by casing-corner separation, while the configuration with a reduced tip loading presented a stronger tip leakage flow that dominated the path to instability.

Significant efforts to improve the stability range of fans and compressors have been made, mostly through the application of casing treatments [18,19] or tip injection [20,21]. These methods have been proved successful in extending the range of safe operation, but their introduction is commonly associated with performance deficits. As a result, their practical application has been limited.

From a blade design perspective, the increased understanding of spike formation mechanisms has not been thoroughly exploited. The tip clearance remains considered as the primary lever that

designers must consider for managing the over tip fluid. While it is indeed a critical parameter, its value also responds to other considerations, such as the desire to minimize the tip rubs experienced in service, the material and stiffness of the blade or manufacturing precision. Such other considerations currently limit the designer's control over stall margin and hence, the design point performance may have to be compromised to achieve sufficient stall range.

The axial momentum flux of the tip leakage fluid across the gap (C_μ) has been found to be a valuable metric to capture the effects of over tip flow on different designs [13, 16]. To enable more control over operability range, in this study, we present a systematic way to design for a target C_μ by considering full-span blade shaping whilst keeping the tip clearance and the design pressure ratio unchanged. By sampling a distribution of different C_μ values, the behavior of stall margin with respect to this quantity is derived, which reinforces the notion that significant control over the operability range (including the onset mechanism) can be achieved through blade design. Based on this concept, it is proposed that tip gap variations are purely a strong driver for C_μ, but that stall characteristics are defined by the latter metric. Moreover, the effect of C_μ on the design point efficiency is also assessed and the trade-off between the stability range and efficiency is discussed in depth. A sensitivity analysis on the design parameters that control C_μ, design point efficiency and design pressure ratio is also performed, leading to an increased understanding of their exchange and which design levers to pull in order to achieve a better overall performance.

COMPUTATIONAL MODEL

This study considers a low speed, high bypass ratio jet engine fan blade, representative of future composite geared turbo-fan, hereby referred to as the *research blade*, as the basis for analysis. This rotor is chosen because it embodies modern design trends resulting in high performance and flow range and it exhibits spike-initiated route to rotating stall. The span of the research blade is about one fourth of a conventional engine-size blade span, as it has been designed to be suitable for rig tests. The rotational speed has been adjusted to emulate the flow physics at the cruise condition and the blade thickness-to-chord ratio is representative of that necessary to maintain the structural integrity of the full scale engine blade.

An experimental campaign has been performed for this blade and the results were employed to
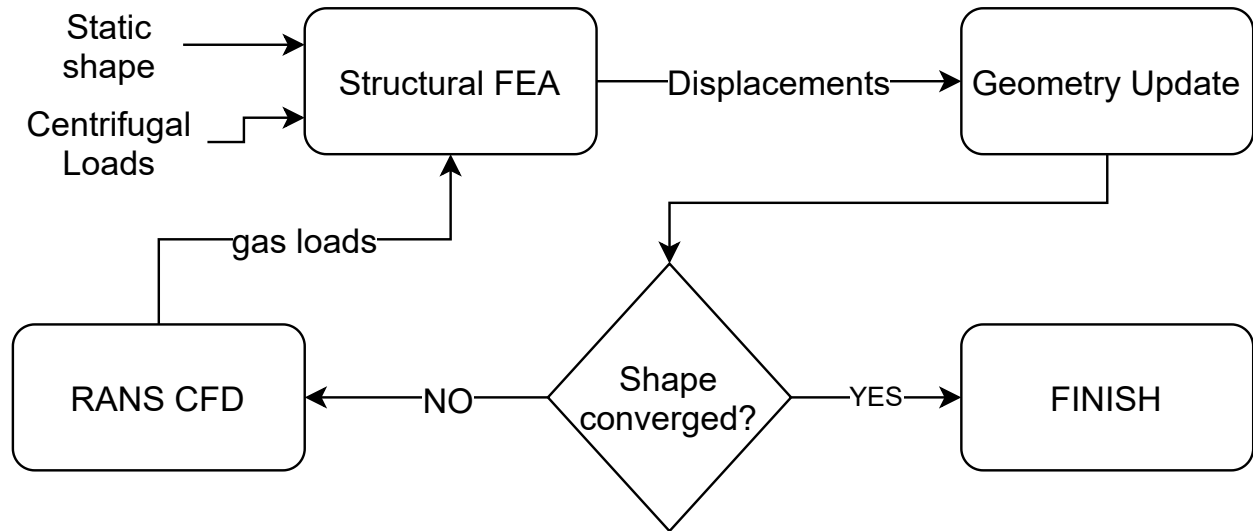
Fig. 1.   RUNNING UP PROCESS OF COLD STATIC BLADE SHAPE.

construct a computational domain that would recreate as accurately as possible the test conditions. A description of the approach taken to maximize the fidelity to which the model simulates the real system is reported in this section.

Blade Geometry

A digital representation of the geometry tested on the rig was constructed by laser scanning the manufactured part and converting the resulting point cloud to CAD-file format through a novel inverse mapping process [22]. Such a geometry profile is representative of the blade as it was manufactured, in other words, cold and static. To obtain the shape of the blade as it is subjected to centrifugal and gas loads, representative of running conditions, a multi-physics iterative process involving a structural finite elements analysis (FEA) model and a computational fluid dynamics (CFD) model was employed for all speeds assessed in this study. A scheme of the process is presented in Fig. 1. Details of the CFD model are of special relevance to the current work and will be addressed at a following section. A description of the FEA model, however, is not provided for the sake of brevity. For every iteration in the process (other than the first one, for which no gas loads are applied), the FEA model is solved to find the shape displacements that result from the application of centrifugal and gas loads to the static shape. The approximating *hot running* geometry that stems from this is simulated with CFD to find the corresponding pressure distribution

on the blade, information which is subsequently fed back to the FEA model for the next iteration. The L_2 norm of the distance field between successive geometries is monitored to determine the convergence. A convergence criterion of $10\mu m$ was achieved in under 7 iterations for the speeds assessed in this study.

As discussed in the introduction, the size of the tip gap is a particularly critical parameter defining the stalling mechanism. The rig was configured with a tip clearance of approximately 1.7% chord, sufficient to guarantee the blade tip would not rub. To ensure the computational model captures the correct behavior, the clearance was measured on the rig and the digital domain applies the corresponding value.

CFD Domain

The computational domain used in this study is shown in Fig. 2. It consists of a single passage for every domain employing periodic boundaries. The model includes the rotor blade, bypass outlet guide vane (BOGV), engine side stator (ESS) and straightener vane (SV). The rotor domain is modeled on a rotating frame, with the the casing, splitter, inlet, exit and a patch of the hub set as stationary surfaces. All blades, hub, splitter and casing surfaces are set as viscous walls. At the inlet, a non reflecting radial profile of total pressure, total temperature, whirl and pitch angles, and turbulence intensity is specified, where the values for these quantities were obtained from the rig test. For the bypass and core exit surfaces, non-reflecting, radial-equilibrium capacity (Φ) exit boundary conditions (BC) are enforced, while mixing planes are employed at the zone interfaces.

The CFD pre-processing makes use of the Rolls-Royce proprietary geometry and meshing software, PADRAM [23]. The structured mesh blocking strategy employed by PADRAM for each zone consists of an H-O-H topology for the blade passage, with H blocks for the upstream and downstream regions, as well as the upper and lower periodic boundaries. The blades are enveloped in an O-mesh while a C-mesh is used for the splitter. For the rotor tip, a butterfly topology is employed. The grid strategy was tailored for the aerodynamic design point (ADP) and employed for all subsequent operating points assessed. The grid spacing on the solid walls is adjusted to produce y^+ values between 1 and 2 on the blade surfaces and lower than 5 on the rotor tip and casing. The radial distribution of nodes in the rotor zone is set such that 90 were placed at the
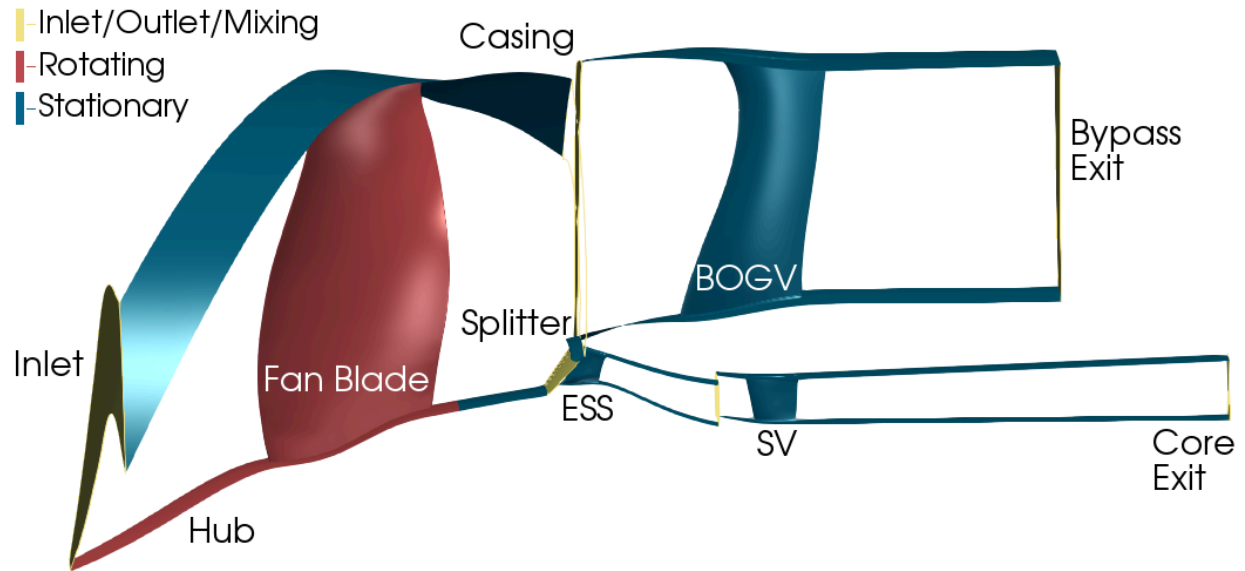
Fig. 2.   ILLUSTRATION OF THE CFD DOMAIN FOR THE RESEARCH BLADE. IMAGE DISTORTED AND NOT TO SCALE.

core exit and 160 at the bypass exit, with 40 of those being located in the tip gap. The downstream stators, in turn, copy the node distribution from the rotor at the interfaces to avoid any radial mesh discontinuities at the mixing planes. The O-mesh applies 30 nodes around the blade surface and 30 additional nodes are placed in the H-mesh blade-to-blade direction. The number of axial nodes for each zone varies based on their actual distance from inlet to exit. The spacing criteria employed is such that the average axial spacing is about 2% axial chord at mid-span.

CFD Solver

While fan stall is inherently an unsteady phenomenon, recent turbulence closure formulations enable performing steady-state numerical simulations until just before the onset of instability [24], leading to a cost-effective means to identify the stall point. This work employs the helicity-corrected Spalart-Allmaras turbulence closure model [25]. It was found that the scaling of the production term based on the local flow helicity promotes an increased resolution of the leakage flow and corner separation, stabilising the computations at lower mass flows and enabling more accurate predictions of the stall point. The improved accuracy in stall point definition was also observed on similar fan blade computations with this turbulence model [16]. Interestingly, in this work, it is also shown that it is possible to accurately predict the different spike formation mechanisms through

steady-state simulations employing this turbulence model, providing an accurate characterisation of stall onset and minimising the need for time-accurate computations. Additional information regarding this turbulence model can be found in the Appendix.

The model is implemented within the Rolls-Royce proprietary CFD code Hydra [26], which was used for all numerical computations in this study. Hydra is an unstructured solver employing an edge-based data structure and convergence acceleration through an element collapsing multi-grid algorithm. A five-stage Runge–Kutta scheme with a block Jacobi preconditioner is employed for pseudo time-stepping when solving the steady-state Reynolds-averaged Navier–Stokes equations (RANS).

Identification of stall point

The fan operating point is controlled in the model through the bypass capacity BC. We define the numerical stall point as the minimum exit capacity for which the CFD solution reaches a steady convergence, as defined by inlet capacity, pressure ratio and bypass isentropic efficiency monitors. The emergence of small amplitude oscillations in the convergence history of any quantity was deemed sufficient to infer the presence of unsteady features and consider the operating point as the onset of instability. The simulations at those conditions are deemed as not-converged. Therefore, the computation of the stall point is performed at the last numerically stable operating condition, just before the onset of instability, and the stalling mass flows reported in this study are representative of the minimum value that would produce a fully steady flow field.

To identify the stall point as efficiently as possible, a bracketing optimization approach was employed following a Fibonacci search method [27], where the final size of the interval was selected to be 0.2% of the ADP capacity. Most stall point estimations converged within 5 to 7 CFD runs.

Model Validation

The aim of this work is to assess the behavior of different fan designs in terms of their ADP performance and stall margin. Additionally, the top of climb (TOC) condition was also selected to monitor the stall margin as it has typically constituted a challenging condition both from an operability and a numerical modelling point of view. To provide confirmation that the model is capturing the correct physics with sufficient accuracy, bypass characteristics were run at two speeds, 95%

and 103%, corresponding to the ADP and TOC speeds respectively, and were compared against experimental results. To throttle from choke to stall the bypass capacity BC was gradually reduced, whilst the core BC was kept at the cruise working line value.
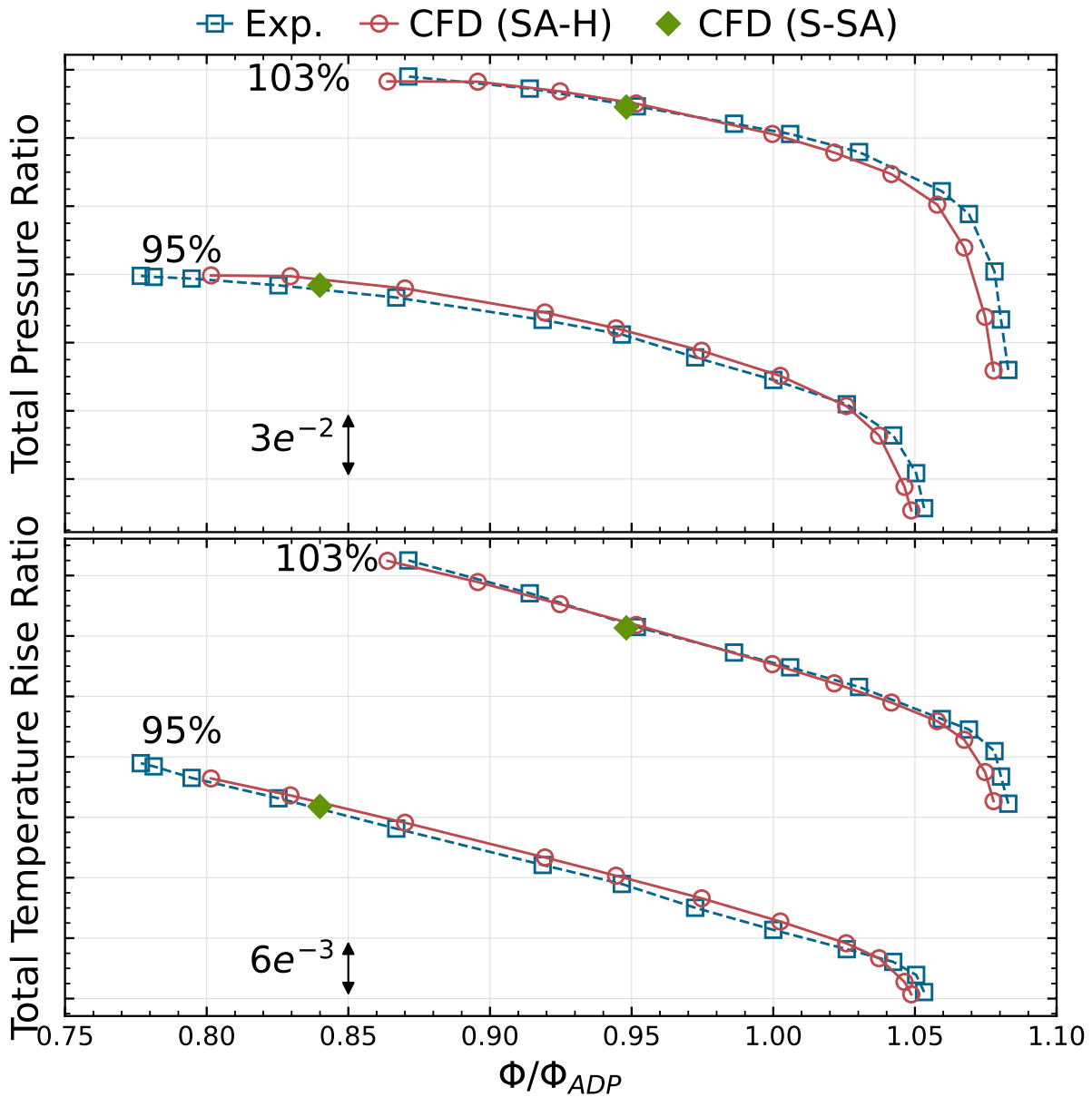

Fig. 3.   VALIDATION OF PERFORMANCE CHARACTERISTICS FOR MODEL AGAINST EXPERIMENTAL DATA.

The characteristic curves are presented in Fig. 3, showing a close agreement between the
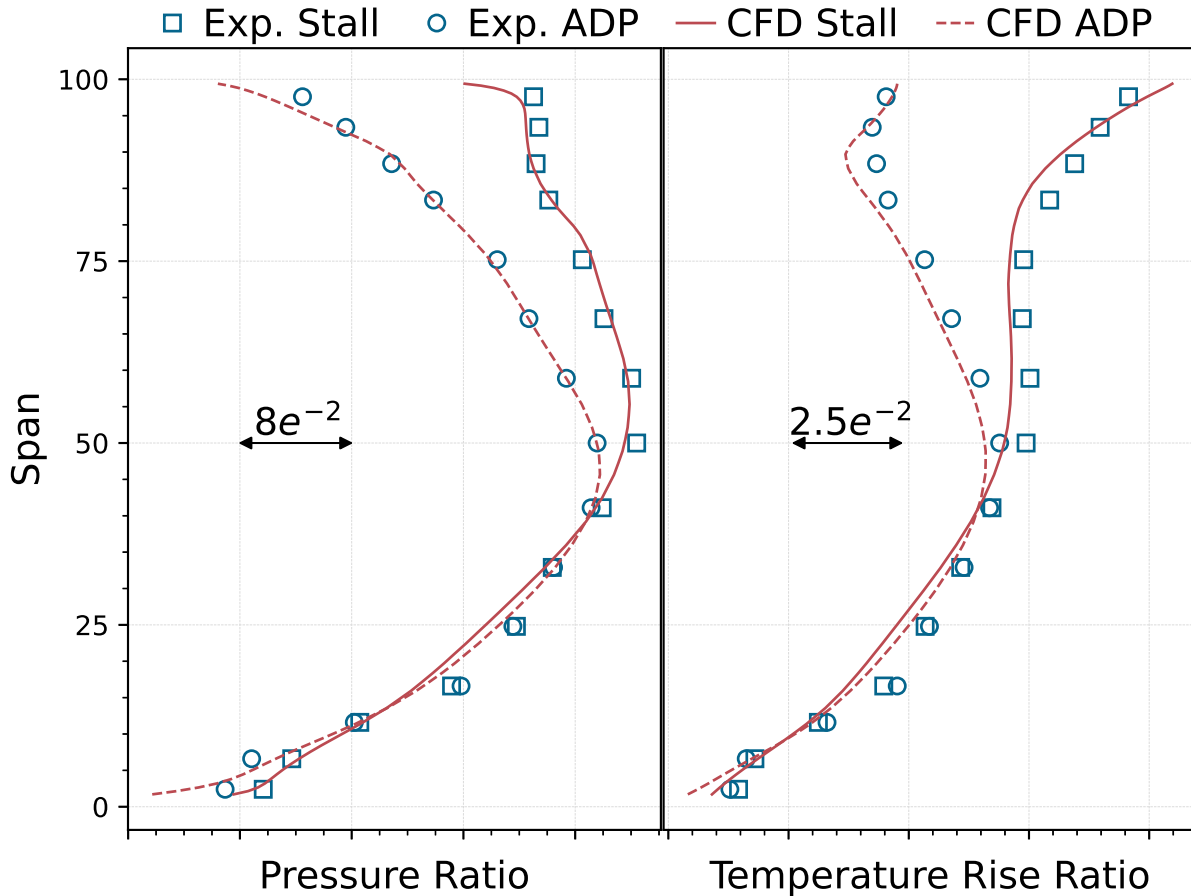
Fig. 4. RADIAL PROFILES AT THE BOGV LE FOR 95% SPEED AT THE ADP AND NEAR STALL CONDITIONS.

helicity-corrected Spalart-Allmaras (SA-H) computations and experimental results in pressure ratio and temperature rise ratio for both speeds assessed. The performance variation as the shaft is sped up from 95% to 103% is captured in the model with negligible deviations with respect to experimental data, denoting an adequate treatment of the gas and centrifugal loads on the blade shape. For the 95% curve, the calculations follow closely the rig results from choke down to a normalized mass flow of 0.8, indicating that the unstalled flow fields are replicated adequately. The stalling mass flow is over-estimated, with the CFD prediction being about 2.4% higher than the experimentally determined value. For the 103% speed, however, the stall margin prediction is closer and the model stalled within 0.6% of the experimental stalling mass flow, while maintaining a close agreement at higher mass flows. The stall margin computations employing the standard

Spalart-Allmaras model (S-SA) are also included in the figure, i.e., the last numerically stable point from the simulation with that model, highlighting the significantly increased accuracy obtained in the computation of this quantity when employing the helicity-corrected term.

The radial profiles of pressure ratio and temperature rise ratio, extracted at the BOGV LE, are shown in Fig. 4 for 95% speed at two conditions, ADP and the CFD stall point. Near the hub, there is a slight under prediction of both metrics at the conditions assessed, whereas the distribution outboard of 25% highlights the close agreement between the CFD model and experimental data. The loading increase on the outer 50% span experimented as the mass flow is reduced from ADP to stall is captured successfully on the pressure and temperature profiles. This is relevant for the current investigation as near stall conditions the shock moves closer to the LE and promotes a thickening of the boundary layer downstream, which in turn, and due to a low axial momentum, tends to migrate outwards. The ability to adequately predict this radial migration of the flow has historically been associated with turbulence modelling. Thus, the validation of the profiles provides confidence that the turbulence model employed is producing adequate radial mixing and that the near stall three-dimensional flow field is captured with sufficient accuracy in steady state simulations.

DESIGN SPACE EXPLORATION

The hypothesis of this research work is that the stall margin and the stall onset mechanism are primarily driven by the axial momentum flux of the tip leakage jet across the gap. To test it, a systematic method to control this feature and characterise its behavior through three-dimensional design is sought. To this end, a flexible control over the geometry under study is essential, while at the same time it remains necessary to maintain adequate generalization to other problems. While free-form deformation or B-splining-based parametrizations would provide increased geometry control, a subsequent analysis would be inherently biased and the location of nodes difficult to reproduce. Therefore, this work makes use of PADRAM's *Engineering Design Parameters*, which are composed of intuitive manipulation handles based on first principles. The degrees of freedom employed, shown in Fig. 5 for an aerofoil section, include *Sweep* (axial movement of the section), *Lean* (circumferential movement of the section), *Skew* (rotation about the section's centroid) and

Leading Edge (LE) and Trailing Edge (TE) *recambering*, as well as two additional parameters that control the *locality* of the recambering. The locality parameters control the chord-wise extent of the camberline alterations such that low values concentrate the changes on the LE/TE and high values propagate them throughout the aerofoil, providing full control over the camberline. While an important design parameter, the blade chord is kept unchanged in the current study to avoid inducing changes that might affect the weight of the system. The parameters are applied on five aerofoil *control sections* uniformly distributed through the blade span - at 0%, 25%, 50%, 75%, 100% - providing a total of 35 degrees of freedom. The value of the deformation applied as a function of the blade span is achieved through smooth cubic B-spline interpolation, with multiple control points via the control sections. The design parameters are gathered in the design vector, $\mathbf{x}$, and its dimensionality is denoted by the letter m, where $m = 35$. The lower and upper bounds that define the ranges of the design space are prescribed based on prior experience with the parametrization, which has been used on previous optimization studies providing sufficient geometry control [28, 29].

AI-Enabled Active Subspaces

To characterise the response of the system to the geometry changes introduced by this parametrization and perform exploratory analyses, this work makes use of AI-Enabled Active Subspaces. A brief description of the methodology is presented here, for a full treatment of the topic the interested reader is referred to [28] and references therein.

We wish to derive a relationship between the design parameters and the quantities of interest (QoIs). While the parametrization selected comprises aerodynamically intuitive shapes, the number of degrees of freedom is nonetheless large and regressing the behavior of any QoI that depends on them is challenging. Therefore, dimension reduction is desired to narrow the scope of the problem and identify a few *dominant* parameters which cause active changes in the QoI. Because of their ability to handle non-conditioned datasets, Active Design Subspaces (ADS) are selected to learn a low-dimensional representation for each QoI.

By performing the eigenvalue decomposition of the QoI's gradient covariance matrix, C, as $C = W\Lambda W^T$, the ADS approach identifies linear combinations of all the components of $\mathbf{x}$ that best
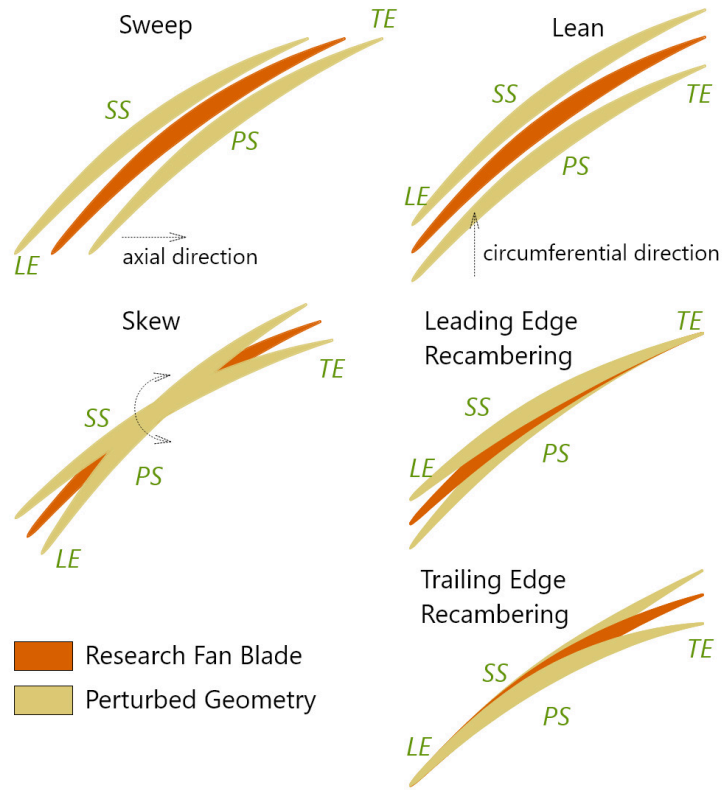
Fig. 5.   DEGREES OF FREEDOM EMPLOYED TO MANIPULATE THE GEOMETRY OF THE FAN BLADE [28].

describe the variability in the function. Essentially it performs a rotation of the coordinate system such that the new directions explain more efficiently the observed variability. The new basis is captured in the eigenvectors of the covariance matrix, W. The eigenvalues, on the other hand, denote the relative importance of each direction and allow partitioning Λ and W as per Eq. 1, such that the most dominant directions are captured in the *active subspace* W_1. Thus, ADS first identifies directions where the function changes most actively and secondly, performs screening of these directions to keep only the k most dominant ones, achieving an efficient dimensionality reduction whilst maintaining all of the original degrees of freedom. The transformation expressed in Eq. 2, called *forward map*, is employed to map the high-dimensional inputs to their low-dimensional active representation, $\mathbf{y}$.

$$\Lambda = \begin{bmatrix} \Lambda_1 & \\ & \Lambda_2 \end{bmatrix}, \ W = [W_1 \ W_2], \ W_1 \in \mathbb{R}^{m \times k} \tag{1}$$

$$\mathbf{y} = W_1^T \mathbf{x} \tag{2}$$

However, learning the ADS requires knowledge on the gradient of the QoI at a large number of locations in the design space, which has traditionally limited the applicability of the method due to the high cost associated with gradient computations. To mitigate this cost, the AI-enabled approach first employs zeroth order information to train a neural network regressor that learns a map from the high-dimensional input space to the QoI and exploits it to estimate the gradients using finite differences, which are subsequently used to construct the ADS covariance matrix. An iterative loop is employed to ensure the subspace is detected with the least amount of samples. Upon identification of the ADS, the forward map is performed for all samples and a secondary neural network is trained on the active directions. This leads to increased predictive accuracy as the ratio of samples to dimensions is increased and the complexity of the function is minimized through the use of $\mathbf{y}$. Therefore, the final network can be employed as a response surface to characterize the response of the system with respect to the design parameters through an enhanced resolution.

EXPLORATORY DESIGN ANALYSIS

The QoIs considered for exploration are the fan total isentropic efficiency, η, the total pressure ratio, PR, and the axial momentum flux of the tip leakage flow normalized by the inlet axial momentum, C_μ. The axial momentum flux is calculated from Eq. 3, where V_{Xjet} is the axial velocity of the leakage jet as it leaves the gap through the suction side, $\dot{m}_{jet}$ is the mass flux through the tip gap, calculated at the suction surface, and $\dot{m}_{inlet}$ and V_{Xinlet} are the mass flow and axial velocity at the passage inlet. This quantity was adopted to investigate the stability of the fan blade,

since, as described in [13, 16], it correlates well with SM. Moreover, unlike SM, whose definition requires identification of the stall point (achieved through 5 to 7 CFD simulations), the value of C_μ is obtained at ADP. As a result, for each design assessed, all metrics were obtained by running a single CFD computation at the ADP.

$$C_\mu = \frac{\dot{m}_{jet} \; V_{Xjet}}{\dot{m}_{inlet} \; V_{Xinlet}} \tag{3}$$

To efficiently explore the design space and obtain the samples necessary to perform AI-Enabled ADS, a trust region strategy was followed based on maximising η, since this is the only QoI that with certainty we wish to maximize. The approach involved constructing sub-regions of the design space where the ranges of the parameters were reduced. By considering a reduced sector, the complexity of the function is inherently mitigated and an accurate regressor can be constructed with a lower number of samples. Initially the sub-region was centered on the datum blade design and spanned 25% of the design space in each direction. A quasi-random DOE based on Sobol' sequences was employed to draw 100 samples. The neural network predictor was constructed for efficiency and a first optimization was performed to maximize it within the sub-region. Next, the center was moved to the location of the optimum and the process repeated. For each iteration, the samples from the previous runs were added and the ranges enlarged to cover the previous sub-regions, such that each step increased the overall sample count and the extension of the design space that was being explored. This strategy avoided placing too many samples on regions of the design space where the fan efficiency was low, while providing an adequate coverage of the remaining section. The optimizations for each sub-region step were performed with a standard elitist genetic algorithm and specified a tight double-bounded constraint on the PR to within $\pm 0.15\%$ of the datum value. The C_μ value was allowed to float freely. The process was stopped once the optimized design fell well within the trust region, conveying little gains from further exploration. Overall, three iterations were required to identify an optimum efficiency point, leading to 300 sampled designs which were employed to construct the final response surfaces.

Table 1. PERFORMANCE METRICS FOR THE RESPONSE SURFACES CONSTRUCTED THROUGH AI-ENABLED ADS.

Metric	Active Dimensions	R^2	MAE
PR	1	0.998	$1.90e^{-4}$
C_μ	2	0.998	$1.77e^{-5}$
η	6	0.995	$9.77e^{-5}$

The performance of the efficiency optimum is of relevance to the current investigation and its design will be addressed accordingly at a later section. For now, focus is set on analyzing the response of the QoIs and deriving generic design rules to provide control over each.
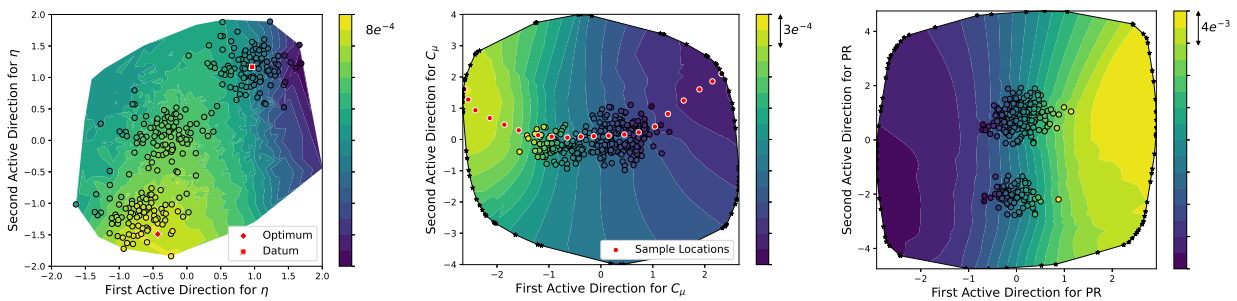

Fig. 6. PERFORMANCE MAPS FOR EFFICIENCY (LEFT), C_μ (CENTER) AND PRESSURE RATIO (RIGHT) SHOWING THE RESPONSE OF THE QoIs IN THE DESIGN SPACE.
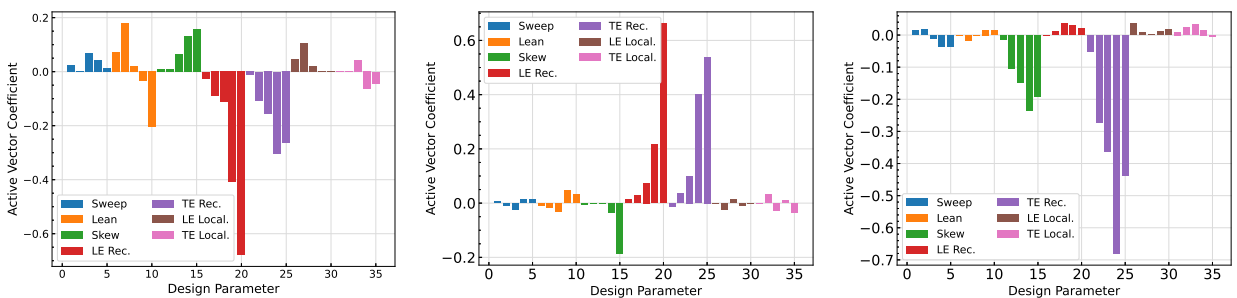

Fig. 7. COEFFICIENT ACTIVATION FOR THE FIRST ACTIVE DIRECTION OF EFFICIENCY (LEFT), C_μ (CENTER) AND PR (RIGHT). HIGHER MAGNITUDE COEFFICIENTS HIGHLIGHT PARAMETERS WITH INCREASED EFFECT.

Based on the decay of their respective eigenvalues, the number of active dimensions to use for each QoI was defined and the response surface models (RSMs) constructed. The predictive

performance of each RSM, evaluated through cross-validation, is presented in Tab. 1, where R^2 stands for coefficient of determination and MAE is the mean-absolute-error. It can be observed that high R^2 values were obtained for all metrics, confirming that the responses of the models follow very close the ones of the real system and therefore any inferences made on them translates well. In addition, the low MAE values measured provide confidence that the true performance of any design is close to the value predicted with these RSM. It is worthy to highlight that generating the training data for the networks required solving a computationally expensive multi-row CFD analysis per sample. The methodology described thus enabled constructing accurate response surfaces with a limited cost. Due to a reduced number training samples, the neural networks employed are *shallow*, consisting of just two hidden layers. As such, their training can be completed without much expense. For the current task, this was completed within 10 minutes on a 16-core CPU.

The fact that all QoIs present such low-dimensional structure, enables visualizing their response through two-dimensional performance maps, shown in Fig. 6, without significant loss of information. The original samples used to construct the response surfaces have been included in the maps and their clustering responds to the movement of the sub-region center. In the efficiency map, to the left of the figure, the movement is particularly evident as this metric was employed to drive the exploration. In addition, the efficiency map has been constructed only in the explored region, as this sector of high-performance was discovered through the trust-region approach. For the other two metrics, the neural networks are employed to extrapolate the data to the corners of the design space, which is represented as a solid line enveloping the contours. The fact that they are low-dimensional and the trend is adequately captured with the ADS promotes accurate extrapolation.

It is worthy to note that the performance maps of Fig. 6 reveal that the change in η and C_μ experienced by the samples does not necessarily induce a variation on the PR, and this was intentionally enforced through the tight constraint specified on the trust-region exploration. The fact that the model employs a BC for the ADP bypass exit capacity implies that the mass flow is constrained as well. Therefore, by constraining the PR and enforcing its value to be effectively *unchanged*, the designs assessed are comparable as they provide the same thrust and share very

similar operating points.

The efficiency map further shows that there is a corridor of high efficiency (towards the center-bottom) where the optimum lies. The exploration driven by the maximization of efficiency has caused a movement across the C_μ subspace, particularly along the first dominant direction, that results in designs with highly variable magnitudes for this quantity. To conceptualize the changes that have caused the performance variation, the active directions can be further exploited to assess the effect that each design parameter has on the variability of the QoIs. The bar graphs in Fig. 7 show the activation coefficient of each parameter in the most dominant direction identified for each function. Recall that the dominant directions are a linear combination of all the original parameters, hence higher magnitude activations highlight parameters with increased effect. Each type of parameter has five bars associated with it, corresponding to the perturbation at the various span-wise locations. The first bar corresponds to the 0% span perturbation, followed by the remaining four bars for perturbations at 25, 50, 75, and 100% span, respectively.

A first glance through Fig. 7 reveals that the active vector coefficients for efficiency are almost the mirror-image of the coefficients for C_μ. This suggests that the two metrics are closely coupled and variations in one translate to variations in the other. This is due to the fact that the interactions of tip leakage jet (expressed by C_μ), with the incoming flow and passage shock are a primary source of losses and blockage [30], thus this feature has a strong effect on efficiency. A closer look at the coefficients for η and C_μ reveal that the primary design lever that drives their value is the tip LE recambering. This implies that the incidence angle and camberline distribution at the LE are responsible for much of the variations detected and have a strong effect on these quantities. The locality of the LE recambering was not detected as significant for either, implying that the camberline distribution is of primary significance only in a small region around LE and full chord control is not particularly necessary. For η, the LE recambering at 75% is the second driver, whilst this parameter does not cause a relatively strong effect on C_μ. In fact, parameters placed at spans other than 100% have a reduced effect on C_μ, highlighting the local nature of the tip leakage flow.

The analysis of the active coefficients reveal that close control over C_μ, and hence the leakage jet, can be achieved by setting focus on the tip aerofoil, while the design of the remainder of the

blade can be driven by other objectives. Consequently, it is noted that the coefficients for LE and TE tip recambering are positive for C_μ and this implies that to move in the positive direction of the map (from left to right in Fig. 6), and thus *decrease* C_μ, positive values must be applied to the recambering parameters. With the parametrization employed, this means *opening up* the tip and taking camber away from the LE and TE. Inversely, closing the tip airfoil and adding camber *increases* the axial momentum of the leakage jet. Some of these changes may appear counter-intuitive. To illustrate, by closing the blade down, the incidence angle at the ADP is reduced and thus the peak suction of the airfoil is mitigated, minimizing lift. This effect can therefore be thought to reduce the mass flow of the leakage jet. However, the higher stagger indicates that the leakage jet is more axial, thereby increasing its axial momentum. In addition, increasing camber also increases lift, which drives more over tip flow.

For other design considerations, it is noted that the most active PR coefficients are mostly contained within the TE recambering type. This is known from first principles since the TE camberline distribution and exit angles control the amount of turning. Blade skew at all spans is secondary in significance for PR while it is not so for the other metrics. Thus, for PR, design focus can be set on defining these parameters. Likewise, blade lean has a moderate effect on efficiency and a very small effect on the other metrics, hence it can be exploited without affecting the PR and leakage jet. Therefore, such parameters that affect mostly a single QoI can be exploited to tune the design and provide a higher degree of control over the desired metric without affecting the performance on other considerations. The following section proposes employing a regularized inverse-mapping methodology to achieve this tight control.

EFFECT OF TIP LEAKAGE FLOW ON STABILITY RANGE

The response surface models constructed based on the active vectors provide increased control over each QoI. This enables producing designs that achieve a desired value of η, PR or C_μ. In this section, an array of uniformly spaced designs is sampled from the C_μ subspace with varying values for this quantity, ranging from the minimum to the maximum possible values attainable with the chosen parametrization. The location of these samples in the zonotope is shown in Fig. 6.

The forward map from Eq. 2 is used to map samples in the high-dimensional space to their

corresponding location in the low-dimensional subspace. This is a well-posed problem yielding a single vector $\mathbf{y}$ for a given vector $\mathbf{x}$. However, the inverse is not true. There are infinitely many $\mathbf{x}$s that solve the inverse map for a given $\mathbf{y}$. Therefore, to find the high-dimensional vectors, $\mathbf{x}^*$, that map to the chosen locations in the C_μ subspace, regularization is needed. This work employs an inverse-map as expressed through Eq. 4.

$$
\begin{aligned}
\mathbf{x}^*(\mathbf{y}) = \underset{\mathbf{x}}{\text{argmin}} \quad & \frac{1}{2}\left\|W_{1_{C_\mu}}^T \mathbf{x} - \mathbf{y}\right\|_2^2 + \lambda \left\|\mathbf{x}\right\|_1 \\
\text{subject to} \quad & \left|\frac{PR(\mathbf{x}) - PR_{datum}}{PR_{datum}}\right| \leq 1.5e^{-3}
\end{aligned}
\tag{4}
$$

The first term of the minimization cost function in Eq. 4 is designed to identify points that, when forward-mapped, fall on the chosen location $\mathbf{y}$. The introduction of the constraint, to produce designs where the PR is within $\pm 0.15\%$ of the datum value, leads to the possibility that there might not be feasible designs that forward map to $\mathbf{y}$. Therefore, the cost function will produce the feasible point that maps *closest* to $\mathbf{y}$ as per the L_2 norm. The cost function of Eq. 4 employs also a LASSO regularization term [31]. This term biases the selection to designs where the least important parameters in the subspace (the ones that do not affect the value of the first term) are pushed to zero. By changing the value of the coefficient λ, this shrinkage effect is strengthened or weakened, thus providing control over the final design. This study assessed an array of λ values, ranging from 10^{-1} to 10^{-4}.

For each sample, the inverse map was solved and the resulting design was simulated with CFD at the ADP condition and the stall point. The Stall Margin (SM) was subsequently calculated as per Eq. 5.

$$
SM = \frac{\Phi_{ADP} - \Phi_{stall}}{\Phi_{ADP}} * 100
\tag{5}
$$

Figure 8 shows the distribution of stall margin as a function of C_μ for the samples assessed.
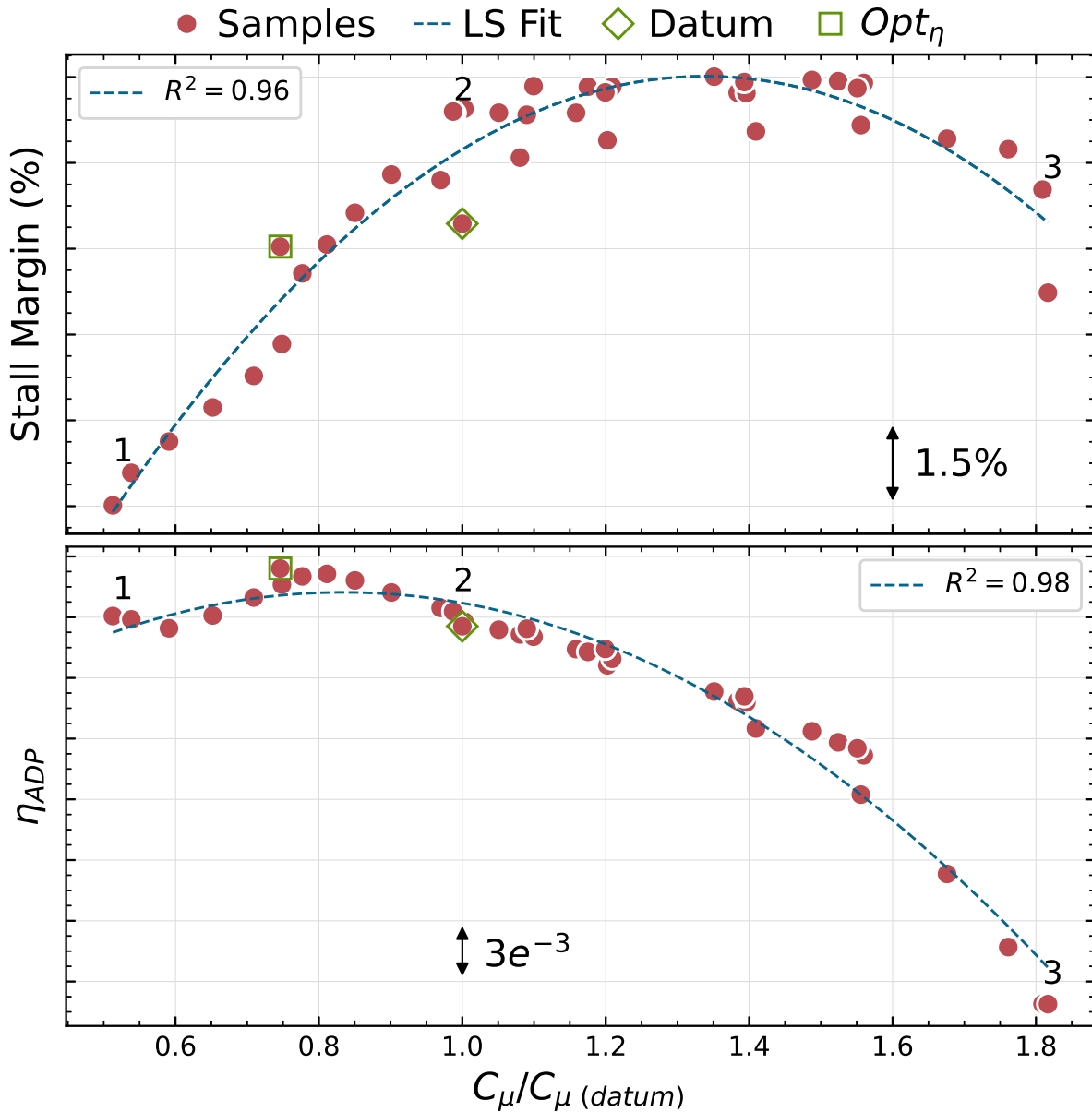
Fig. 8.   STALL MARGIN AND ADP EFFICIENCY VS TIP LEAKAGE AXIAL MOMENTUM FLUX NORMALIZED BY DATUM VALUE. THE QOIs PRESENT A QUADRATIC RESPONSE TO CHANGES IN AXIAL MOMENTUM.

It can be observed that C_μ is a very strong driver for SM and that is has a quadratic response, as indicated by a high coefficient of determination (0.96) for a least-squares (LS) second order polynomial fit to the data. Three regions of distinctive response are noted and representative designs indicated by the numbers 1, 2 and 3 in the figure. At low C_μ values, corresponding to a mitigated leakage jet (point 1), the SM is initially low. Shock-boundary layer interactions take
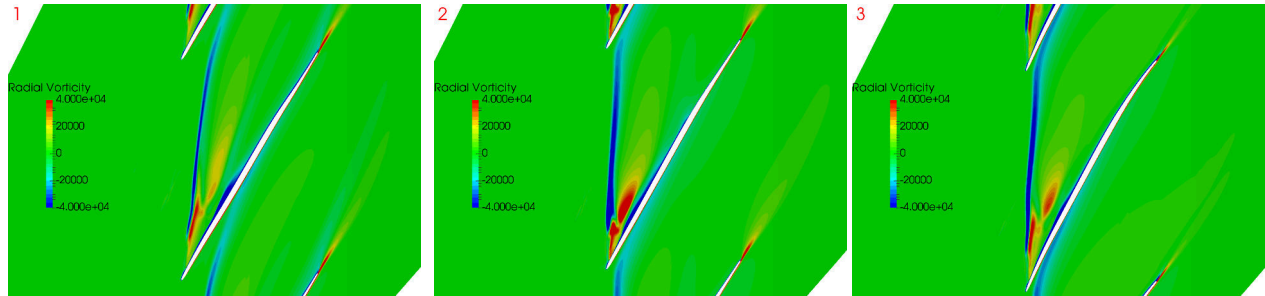
Fig. 9. CONTOURS OF RADIAL VORTICITY AT STALL FOR DESIGN 1 (LEFT), 2 (CENTER) AND 3 (RIGHT) AT 95% SPAN. THE ENHANCEMENT OF THE LEAKAGE JET INITIALLY SUPPRESSES THE CORNER SEPARATION LEADING TO INCREASED STALL RANGE. FURTHER INCREASES IN ITS STRENGTH CAUSE IMPINGEMENT ON ADJACENT BLADE'S PRESSURE SURFACE AND EARLY SPILLAGE.

precedence and, due to its low energy, the boundary layer separates downstream of the shock, causing blockage that extends well into the passage, as it can be visualized by the radial vorticity contours of Fig. 9(a), which are taken at 95% span. While the leakage jet cannot be entirely eliminated (for non-zero tip gaps), its effect can be greatly mitigated causing the spike inducing mechanism to be separation-dominated. As the C_μ is increased beyond this region, the leakage jet is enhanced and energizes the boundary layer, suppressing the separation and alleviating the blockage, thus contributing to an increase in SM. The mechanism switches from being primarily separation-dominated to being leakage-jet dominated, although there is still some separation-induced blockage, as it can be seen from Fig. 9(b), which corresponds to point 2 in Fig. 8. This is consistent with stall onset at the optimal tip gap value identified in [13]. Further increases in the leakage jet strength promote this feature to become dominant and impinge on the adjacent blade's pressure side, promoting flow reversal and early spillage, as shown in Fig. 9(c) for point 3.

The ideal Mach number distributions, shown in Fig. 10, further clarify how the design parameters are affecting the behavior of the flow in these distinctive regions. Going from design 1 to design 2, the camber has been increased at the LE, strengthening the suction spike, which in turn drives more flow over the tip. In addition, the blade has been closed down, resulting in an overall lower incidence that reduces the pre-shock Mach number. The combination of a weaker shock and a more energetic boundary layer, produces a more uniform loading and increases lift. Additional mass flow through the gap, driven by local LE recambering, and a more axial jet resulting from closing the blade lead to design 3, which promotes the impingement of the adjacent blade's
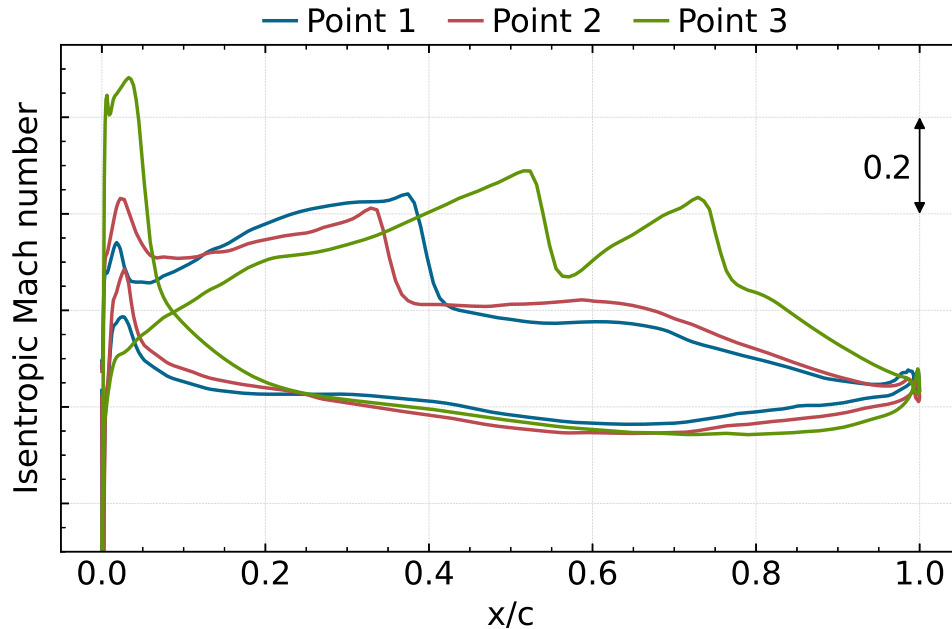
Fig. 10. ISENTROPIC MACH NUMBER DISTRIBUTIONS AT 95% SPAN.

leakage jet on the pressure surface, causing a significant loss of pressure at the LE and greatly accentuating the pressure side spike. The lower incidence delays the peak suction point and the shock gets sucked into the passage, developing a double-shock structure which is detrimental to stability and performance.

The effect of C_μ on ADP efficiency is also shown in Fig. 8. As previously mentioned, these two metrics are tightly coupled and this figure confirms this. The effect of C_μ is again quadratic with a coefficient of determination of 0.98. The region of low jet momentum is associated with intermediate efficiency values, as the shock-induced separation causes loss. The suppression of the separation promotes an efficiency increase, while designs with overly strengthened leakage jet perform the poorest, due to the detrimental effects induced by the mixing of the leakage jet with the incoming flow, as well as passage shock-jet interactions. Moreover, without having actively controlled the leakage jet during the process, the efficiency optimization has produced a design where the C_μ was naturally placed in the region of high-performance, which corresponds to normalized C_μ values of around 0.75, as it can be seen from Fig. 8. While this design is high-performing at the ADP, its SM is slightly lower than the datum and indeed far from optimal in that sense. There

is thus a trade-off between efficiency and stability range, which can be mostly driven by controlling the axial momentum of the leakage flow.

The η-optimized design achieves an efficiency improvement of 0.3% and a reduction in SM of 0.4%. Figure 11 presents a top view of the datum and the efficiency-optimized design. It can be appreciated that, predominantly, the optimized design features a lean of the tip towards the pressure side and the LE has been opened-up. As such, the optimizer has focused on mitigating the leakage jet (through LE recambering) and has further enhanced the performance by applying a parameter which did not affect this flow feature (lean).

Fig. 11.   TOP VIEW OF DATUM AND EFFICIENCY-OPTIMIZED DESIGNS.

It can be noticed from Fig. 8 that, while slightly lower than the datum's value, the optimized design's SM is higher than other points that have the same C_μ. In fact, the figure reveals a number of designs that have the same C_μ but different SM values. This suggests that C_μ is a strong driver for SM, but there are other parameters that also cause a significant effect. The ADP efficiency, on the other hand, remains approximately constant for constant C_μ values. As such, there are designs

(such as point 2 in Fig. 8) that have efficiency values very close to the datum's, but a significantly increased stability. The different designs at constant axial momentum values were constructed by employing varying levels of the regularization coefficient in Eq. 4, and thus incorporate different design considerations. By analysing the different samples that yield higher SM, further design principles can be derived.
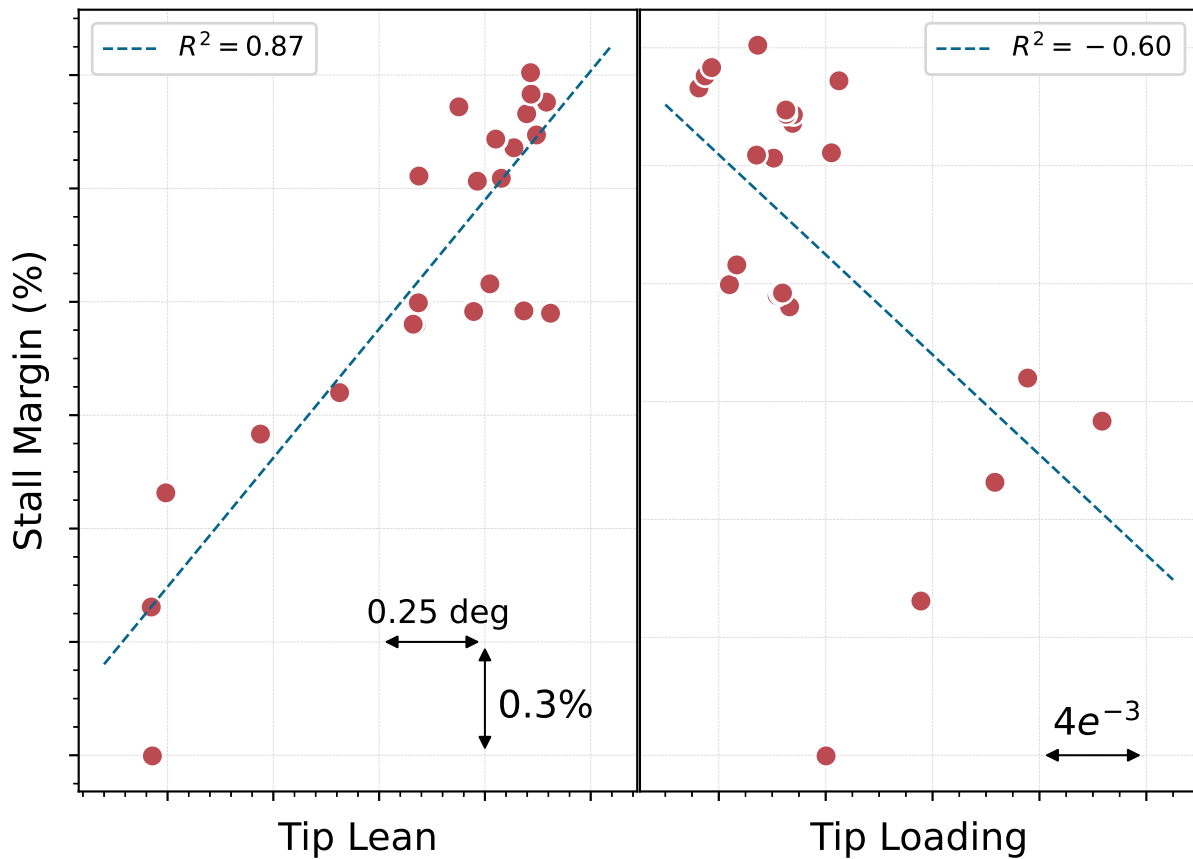

Fig. 12. SECONDARY DESIGN DRIVERS FOR STALL MARGIN. FOR A GIVEN AXIAL MOMENTUM, OFF-LOADING THE TIP AND APPLYING LEAN TOWARDS PRESSURE SIDE PRODUCE INCREASED STABILITY.

Focus is now set on the region of normalized C_μ between 1.0 and 1.6, where the additional designs have been constructed. It was found that the main difference between these was the tip loading, measured as the average pressure ratio on the upper 5% span, and the level of lean applied to the tip aerofoil. Figure 12 shows the correlation of these two design considerations with

SM. It can be noticed that tip lean presents the higher correlation, and increasing levels promote an increase in SM. Tip lean is calculated as a circumferential rotation of the tip section (Fig. 5), where positive values are measured in the direction of rotation of the blade. Therefore, the correlation reveals that leaning the tip aerofoil towards the pressure side leads to increased stability for given C_μ values. This is observed for the efficiency-optimized design as well (Fig. 11). With respect to the tip loading, the correlation with SM is not as strong but it remains considerable. The results suggest that off-loading the tip generally improves the stability margin for constant C_μ values.

RESULTS AT TOP OF CLIMB

The previous analysis has been performed at 95% speed, which corresponds to the ADP speed. However, as already mentioned, the TOC is a key condition to assess the operability range. Therefore, this condition was simulated for a few designs from Fig. 8 ranging from low to high values of C_μ. It is worth noting that the derivation of these designs was performed for 95% speed and therefore the ranges of C_μ quoted in this section are not necessarily the minimum and maximum possible values that can attained at this speed. Moreover, the blade shapes at 103% have been obtained by employing the aforementioned *running-up* process.

Figure 13 shows the variation in SM and efficiency with respect to C_μ for some designs as their are sped up from 95% to 103% speed. To make the results at the two speeds comparable, the data has been normalized by the datum value at the corresponding speed. This figure reveals that the leakage jet still promotes a quadratic response on both metrics at increased speeds. However, the variation at 103% is much more pronounced and the trend falls-over more rapidly at high C_μ values than it does at the ADP speed, suggesting the system is less robust to variable C_μ at high speeds. Moreover, for SM, the data indicates that operating on normalized C_μ values that provide optimum stability at ADP actually leads to operating at the condition "3", identified previously, at TOC speed, with a poor stability performance. There is thus a trade-off in the tip leakage strength for optimal stability at different speeds. For efficiency, on the other hand, the optimal axial momentum for maximum performance is consistent at the two speeds, indicating there is no real trade-off in this metric as the fan is sped-up with respect to the axial momentum.
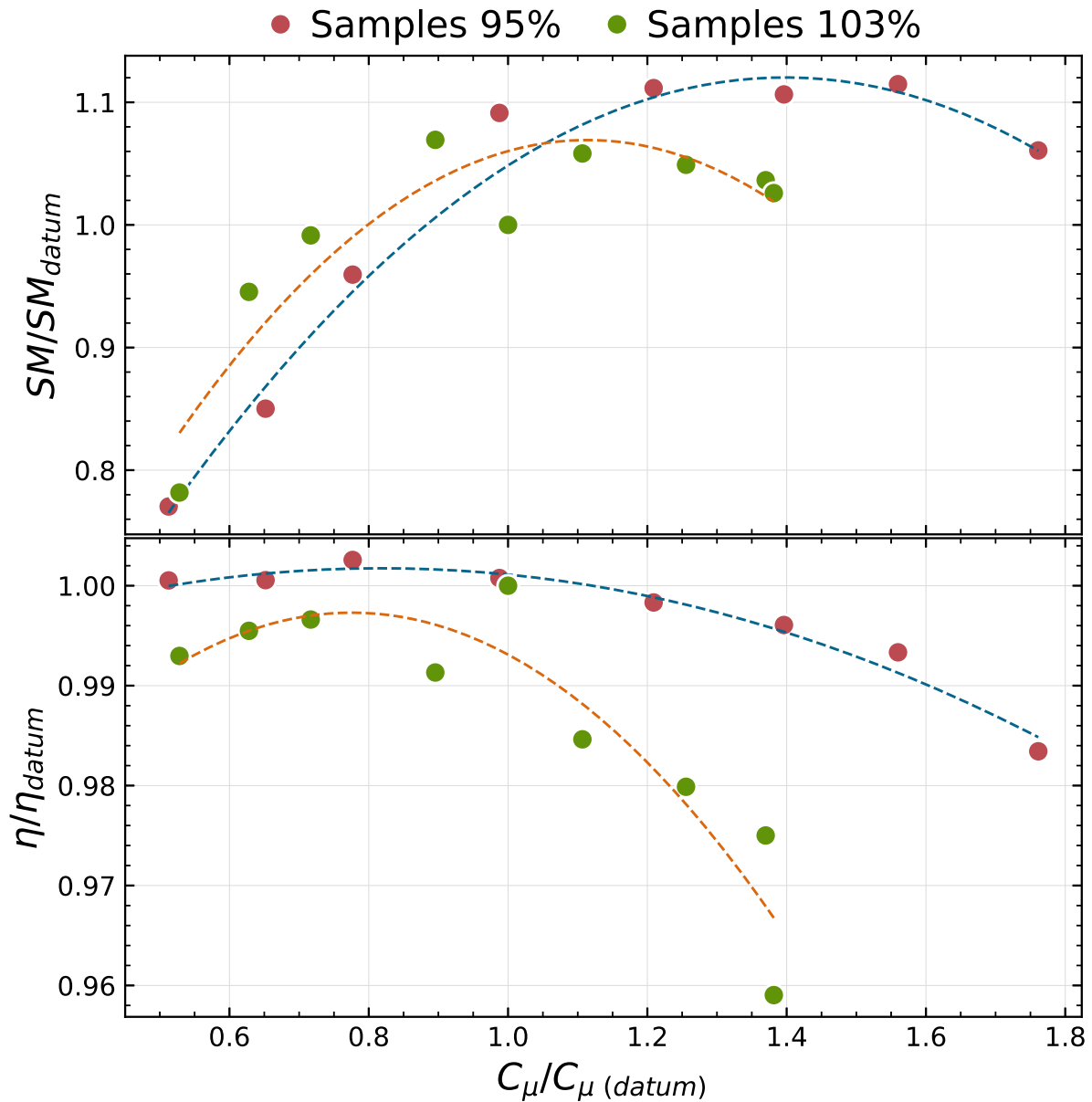
Fig. 13. VARIATION OF FAN PERFORMANCE VS AXIAL MOMENTUM FLUX AS THE SPEED IS INCREASED.

CONCLUSIONS

This study has focused on the effect of tip leakage axial momentum flux on design point efficiency and stability range for an axial fan representative of future composite geared turbo-fan engines. The analysis has been driven by the use of a high-fidelity computational model which has been validated against experimental data. The simulations performed were steady-state and

involved the use of the helicity-corrected Spalart-Allmaras turbulence model. It has been shown that, through this model, sufficient resolution can be obtained for the calculation of the stalling mass flow and the onset mechanism, minimising the need for time-accurate computations.

Furthermore, a design and analysis methodology has been employed, which enabled building highly accurate meta-models for efficiency, pressure ratio and stall margin with a reduced computational cost. Through its application, the characterization of the system and the interactions between the quantities of interest was achieved using only 300 samples for 35-dimensional input parameters.

A quadratic response has been detected for both efficiency and stability with respect to the tip leakage jet's axial momentum. Three regions of distinctive behaviour are observed. At low axial momentum values, the leakage jet is mitigated and shock-boundary layer interactions dominate the exchange. The stall onset mechanism is driven by separation-induced blockage and the efficiency is intermediate, responding to losses originated through the separation. As the leakage jet is strengthened, however, it initially suppresses the separation and leads to an increase in both stability and efficiency. The stall onset mechanism switches to being primarily leakage jet-dominated. Nonetheless, further strengthening of the leakage flow promote an increased effect of this feature which becomes detrimental to stability, by impinging on the adjacent's blade pressure side and early spillage ahead of the leading edge, and efficiency, by inducing increased mixing losses. The optimal setting for efficiency differs from the one for optimal stability but the trade-off can be exploited through controlling the axial momentum. This trend has been verified for higher speeds corresponding to the engine's top of climb condition. However, it was revealed that the optimal leakage momentum for maximum stability varies as the shaft speed is increased, and there is also a trade-off for the stability margin at different speeds, indicating compromises are required to balance ADP and TOC stability.

Blade design rules for increased over-tip flow control have been derived which promote local tuning of the tip aerofoil while the remainder of the blade can be designed for a target pressure ratio. It has been shown that opening the tip and taking camber away from the leading edge are strong levers to mitigate the leakage jet. Additional stability enhancements beyond optimal axial

momentum have been shown to be attainable through off-loading the blade tip and leaning the tip towards the pressure side.

DATA AVAILABILITY STATEMENT

The authors attest that all data for this study are included in the paper.

ACKNOWLEDGEMENTS

APPENDIX

The helicity-corrected Spalart-Allmaras model was first introduced by Liu *et al*. [25] on 2011. Different flavours of the correction have been proposed in the literature, but the implementation employed in this work stems from the original definition. The source term in the S-SA model is augmented as per Eq. 6, where the helicity is computed from Eq. 7. The velocity, $\mathbf{u}$, and vorticity, ω, in the equations are measured in the absolute frame of reference. The value of the constants is taken from [25].

$$\tilde{S}_{SA-H} = (1 + C_{h_1} h^{C_{h_2}})\omega + \frac{\tilde{\nu}}{\kappa^2 d^2} f_{\nu_2} \tag{6}$$

$$h = \frac{|\mathbf{u} \cdot \omega|}{\|\mathbf{u}\| \, \|\omega\|} \tag{7}$$

NOMENCLATURE

ADP   Aerodynamic Design Point.

ADS   Active design subspace.

BC   Boundary Condition.

BOGV Bypass Outlet Guide Vane.

C   Function's gradient covariance matrix.

CFD   Computational Fluid Dynamics.

ESS   Engine Side Stator.

FEA   Finite Elements Analysis.

LASSO Least absolute shrinkage and selection operator.

LE   Leading edge.

LS   Least squares.

MAE   Mean absolute error.

PR   Pressure ratio.

QoI   Quantity of interest.

RSM   Response surface mode.

SA-H Helicity-corrected Spalart-Allmaras turbulence model.

SM   Stall margin.

S-SA Standard Spalart-Allmaras turbulence model.

SV   Straightener Vane.

TE   Trailing edge.

TOC   Top of Climb condition.

R^2 Coefficient of determination.

W   Eigenvector matrix of C.

Λ Eigenvalue matrix of C.

Φ Flow capacity $= \dot{m}\sqrt{T_0}/p_0$.

$\dot{m}$ Mass flow.

T Mass-averaged total temperature.

p Mass-averaged total pressure.

C_μ Tip leakage flow axial momentum flux.

η Isentropic efficiency.

λ LASSO regularization coefficient.

REFERENCES

[1] McDougall, N. M., Cumpsty, N. A., and Hynes, T. P., 1990. "Stall Inception in Axial Compressors". *Journal of Turbomachinery,* **112**(1), 01, pp. 116–123.

[2] Day, I. J., 1993. "Stall Inception in Axial Flow Compressors". *Journal of Turbomachinery,* **115**(1), 01, pp. 1–9.

[3] Moore, F. K., and Greitzer, E. M., 1986. "A Theory of Post-Stall Transients in Axial Compression Systems: Part I—Development of Equations". *Journal of Engineering for Gas Turbines and Power,* **108**(1), 01, pp. 68–76.

[4] Camp, T. R., and Day, I. J., 1998. "A Study of Spike and Modal Stall Phenomena in a Low-Speed Axial Compressor". *Journal of Turbomachinery,* **120**(3), 07, pp. 393–401.

[5] Garnier, V. H., Epstein, A. H., and Greitzer, E. M., 1991. "Rotating Waves as a Stall inception Indication in Axial Compressors". *Journal of Turbomachinery,* **113**(2), 04, pp. 290–301.

[6] Weigl, H. J., Paduano, J. D., Frechette, L. G., Epstein, A. H., Greitzer, E. M., Bright, M. M., and Strazisar, A. J., 1998. "Controls and Diagnostics Committee: Active Stabilization of Rotating Stall and Surge in a Transonic Single-Stage Axial Compressor". *Journal of Turbomachinery,* **120**(4), 10, pp. 625–636.

[7] Spakovszky, Z. S., van Schalkwyk, C. M., Weigl, H. J., Paduano, J. D., Suder, K. L., and Bright, M. M., 1999. "Rotating Stall Control in a High-Speed Stage With Inlet Distortion: Part II—Circumferential Distortion". *Journal of Turbomachinery,* **121**(3), 07, pp. 517–524.

[8] Williams, T. S., Hall, C. A., and Wilson, M., 2020. "Low pressure ratio transonic fan stall with radial distortion". *Journal of the Global Power and Propulsion Society,* **4**, pp. 226–237.

[9] Weichert, S., and Day, I., 2013. "Detailed Measurements of Spike Formation in an Axial Compressor". *Journal of Turbomachinery,* **136**(5), 09.

[10] Vo, H. D., Tan, C. S., and Greitzer, E. M., 2008. "Criteria for Spike Initiated Rotating Stall". *Journal of Turbomachinery,* **130**(1), 01.

[11] Pullan, G., Young, A. M., Day, I. J., Greitzer, E. M., and Spakovszky, Z. S., 2015. "Origins and Structure of Spike-Type Rotating Stall". *Journal of Turbomachinery,* **137**(5), 05.

[12] Dodds, J., and Vahdati, M., 2015. "Rotating Stall Observations in a High Speed Compressor—Part I: Experimental Study". *Journal of Turbomachinery,* **137**(5), 05.

[13] Hewkin-Smith, M., Pullan, G., Grimshaw, S. D., Greitzer, E. M., and Spakovszky, Z. S., 2019. "The Role of Tip Leakage Flow in Spike-Type Rotating Stall Inception". *Journal of Turbomachinery,* **141**(6), 02.

[14] Choi, M., Vahdati, M., and Imregun, M., 2011. "Effects of Fan Speed on Rotating Stall Inception and Recovery". *Journal of Turbomachinery,* **133**(4), 04.

[15] Choi, M., Smith, N. H. S., and Vahdati, M., 2012. "Validation of Numerical Simulation for Rotating Stall in a Transonic Fan". *Journal of Turbomachinery,* **135**(2), 11.

[16] Kim, S., Pullan, G., Hall, C. A., Grewe, R. P., Wilson, M. J., and Gunn, E., 2019. "Stall Inception in Low-Pressure Ratio Fans". *Journal of Turbomachinery,* **141**(7), 02.

[17] Inoue, M., Kuroumaru, M., Tanino, T., and Furukawa, M., 1999. "Propagation of Multiple Short-Length-Scale Stall Cells in an Axial Compressor Rotor ". *Journal of Turbomachinery,* **122**(1), 02, pp. 45–54.

[18] Cevik, M., Duc Vo, H., and Yu, H., 2016. "Casing Treatment for Desensitization of Compressor Performance and Stability to Tip Clearance". *Journal of Turbomachinery,* **138**(12), 06. 121008.

[19] Rolfes, M., Lange, M., Vogeler, K., and Mailach, R., 2017. "Experimental and Numerical Investigation of a Circumferential Groove Casing Treatment in a Low-Speed Axial Research Compressor at Different Tip Clearances". *Journal of Turbomachinery,* **139**(12), 10. 121009.

[20] Li, J., Lin, F., Tong, Z., Nie, C., and Chen, J., 2014. "The Dual Mechanisms and Implementations of Stability Enhancement With Discrete Tip Injection in Axial Flow Compressors". *Journal of Turbomachinery,* **137**(3), 10. 031010.

[21] Wang, W., Liu, B., Lu, J., Feng, J., Chu, W., and Wu, Y., 2022. "Comparative Study of Tip

Injection in a Transonic and Subsonic Compressor". *Journal of Turbomachinery,* **144**(6), 02. 061009.

[22] Shahpar, S., 2020. "Building Digital Twins to Simulate Manufacturing Variation". *Proceedings of the ASME Turbo Expo,* **8**, 09. Paper No. GT2020-15263.

[23] Milli, A., and Shahpar, S., 2012. "Padram: Parametric design and rapid meshing system for complex turbomachinery configurations". *Proceedings of the ASME Turbo Expo,* **8**, 06. Paper No. GT2012-69030.

[24] Lee, K.-B., Wilson, M., and Vahdati, M., 2018. "Validation of a Numerical Model for Predicting Stalled Flows in a Low-Speed Fan—Part I: Modification of Spalart–Allmaras Turbulence Model". *Journal of Turbomachinery,* **140**(5), 04.

[25] Liu, Y., Lu, L., Fang, L., and Gao, F., 2011. "Modification of spalart–allmaras model with consideration of turbulence energy backscatter using velocity helicity". *Physics Letters A,* **375**(24), pp. 2377–2381.

[26] Lapworth, L., 2004. "Hydra-cfd: A framework for collaborative cfd development". *International Conference on Scientific and Engineering Computation (IC-SEC)*, 07.

[27] Ferguson, D. E., 1960. "Fibonaccian searching". *Commun. ACM,* **3**(12), dec, p. 648.

[28] Lopez, D. I., Ghisu, T., and Shahpar, S., 2021. "Global Optimization of a Transonic Fan Blade Through AI-Enabled Active Subspaces". *Journal of Turbomachinery,* **144**(1), 09.

[29] Ghisu, T., Lopez, D. I., Seshadri, P., and Shahpar, S., 2021. "Gradient-enhanced least-square polynomial chaos expansions for uncertainty quantification and robust optimization". *AIAA AVIATION 2021 FORUM*, 08.

[30] Biollo, R., and Benini, E., 2009. "Shock/boundary-layer/tip-clearance interaction in a transonic rotor blade". *Journal of Propulsion and Power,* **25**(3), pp. 668–677.

[31] Tibshirani, R., 1996. "Regression shrinkage and selection via the lasso". *Journal of the Royal Statistical Society: Series B (Methodological),* **58**(1), pp. 267–288.

2022-09-19

Extending highly loaded axial fan operability range through novel blade design

Lopez, Diego I.

American Society of Mechanical Engineers